# Opposing Effects of Amphetamine and Eticlopride on Striatal Fast-Spiking Interneuron Firing Rate

by

Alex Wiltschko

A Thesis Submitted in Partial Fulfillment of the

Requirements for the Degree of Bachelor of Science

With Honors in Neuroscience from the

University of Michigan

2009

Advisor: Dr. Joshua Berke

## Abstract

The basal ganglia are a set of subcortical nuclei needed for proper action selection and behavior. Their dysfunction can lead to serious disorders of movement and motivation, such as Tourette's syndrome and Parkinson's disease. Striatal fast-spiking interneurons (FSIs) contribute to normal action selection by shaping local information processing in the striatum. As part of ongoing investigations into striatal microcircuitry, I first developed a new data analysis technique that increases our ability to detect and record different striatal cells types. I then applied this technique during an investigation of how striatal cells are affected by a psychostimulant (amphetamine) or an antipsychotic (eticlopride). These drugs are known to cause behavioral/ psychological changes largely via their effects in the striatum. However, exactly how they do so on the microcircuit level is unknown. We found opposing effects on FSI firing rates for these two clinically important drugs. Amphetamine significantly increased mean FSI firing rate, while eticlopride decreased it. These findings are relevant to understanding the neural effects of systemic drug treatments for basal ganglia disorders.

Contents

This thesis has two chapters. In the first, I develop a filtering method that preserves waveform shapes in extracellular recordings. This part has been published in the Journal of Neuroscience Methods (Wiltschko et al., 2008).

Using this method to preprocess striatal electrophysiology data, I then conducted a simple experiment to assess the changes in firing rates of striatal fast-spiking interneurons and medium-spiny neurons after treatment of a psychostimulant, amphetamine, and an antipsychotic, eticlopride. This chapter is a manuscript in preparation.

# Chapter 1: Wavelet Filtering Before Spike Detection Preserves Waveform Shape

The removal of unwanted frequencies and artifacts is essential in the analysis of electrophysiological data, especially where the data of interest are the time stamps of neuron action potentials, also called "spikes." In addition to high amplitude spikes, typical electrode signals include local field potentials (LFPs), instrument noise, and spikes from neurons too distant from the recording site to be effectively discriminated. An ideal filtering technique would preserve only discriminable spikes without distorting their waveforms, since differences in waveform shape are useful in clustering and also provide an important source of information about neuronal phenotypes (e.g. Csicsvari et al., 1998**;** Barthó et al., 2004; Berke et al., 2004). Filters commonly used in electrophysiology, such as the Butterworth filter, can be fast to compute and possess a maximally flat frequency response (Butterworth, 1930). However, they possess the undesirable side-effect of distorting the time-domain, e.g. the shape of action potentials.

After the data are filtered, they are usually thresholded to locate spike events, and then certain features of the extracted spikes are used in a manual or semi-automated clustering procedure (Lewicki, 1998). The features to be used in clustering can include spike amplitude, valley width, principal components or wavelet decomposition coefficients. Wavelets have recently gained notice as a powerful tool for signal analysis in the neurosciences and have been applied in a myriad of ways, including spike detection (Hulata et al., 2002; Nenadic and Burdick, 2005), cell classification (Cesar and Costa, 1998; Letelier and Weber, 2000; Quiroga et al., 2004) and EEG/LFP analysis (Clarençon et al., 1996; Adeli et al., 2003; Markazi et al., 2006; Berke et al., 2008). Here, we apply wavelet filtering to "raw" (wide-band) electrode signals as a

preprocessing stage before spike detection and sorting. This approach accurately maintains waveform shape while removing low frequency field potentials and noise artifacts. We demonstrate benefits for the later stages of spike discrimination, compared to the standard Butterworth bandpass filter.

## Method

Algorithms were implemented in the Python language (van Rossum, 1995) using the modules NumPy (Oliphant, 2006), SciPy (for Butterworth filter, as implemented by Jones et al., 2001), Modular toolkit for Data Processing (for principal components analysis (PCA), as implemented by Berkes and Zito, 2007), and PyWavelets (for wavelet transforms, as implemented by Wasilewski, 2006). Algorithms were duplicated when necessary in Matlab for speed comparisions, using the Wavelet and Signal Processing toolboxes (Misiti et al., 2000). All computations were performed on an AMD Athlon 2.2 GHz Windows XP machine with 4 GB of RAM. Electrophysiological data were obtained from tetrodes implanted in two awake freely-moving animals (one rat, one mouse). For the rat, 46 cells across 5 tetrodes from two separate recording sessions were isolated in the striatum, including 30 presumed medium-spiny projection cells (Berke et al., 2004). For the mouse, 20 cells were isolated from 2 tetrodes in a single session from dorsal hippocampus area CA1, including 17 presumed pyramidal cells. In both cases signals were recorded continuously at 31250Hz/channel with hardware filtering with a passband of 1Hz to 9000Hz. Spikes (shown with negative voltage up) were sorted manually using Offline Sorter (Plexon Inc). For comparison of filter performance we used a 4th order Butterworth bandpass filter, with a passband from 300 Hz to 6000 Hz, typical settings for neurophysiology filters. For analyses and visualization, spikes were interpolated by a factor of

four then realigned at their peaks. They were then downsampled to their original sampling frequency of 31250Hz.

*The Wavelet Filter*

We used wavelet multi-level decomposition and reconstruction (WMLDR) as the core of our filter. There are many different names for this procedure, including fast wavelet transform, fast orthogonal wavelet transform, multiresolution algorithm, and pyramid algorithm (Addison, 2002). The algorithm is represented visually in Figure 1 (for further information, see Daubechies, 1992 or Addison, 2002). First, the signal is decomposed into frequency sub-bands (Fig. 1A; Hu et al. 2006) by separate iterative convolution with high- and low-pass wavelet decomposition filters (Fig. 1C). For our application, we used pre-computed values of the Daubechies 4 wavelet (Daubechies, 1988), as provided by the Matlab wavelet toolbox and the PyWavelets Python module. The coefficients containing the higher frequencies of the signal are saved at each iteration $i$ as *detail coefficients*, labeled as $cD_i$. The coefficients containing the lowest frequencies, the *approximation coefficients,* are labeled $cA_n$. Table 1 shows the frequency content of each coefficient set at levels 1-6. The signal is subsequently reconstructed by iteratively convolving the approximation coefficients with the low-pass reconstruction filter, convolving the detail coefficients with the high-pass reconstruction filter and summing the results (Fig. 1B). The reconstruction filters are the time-inverses of the decomposition filters (Fig. 1D), and therefore provide a zero-phase-lag reconstruction (for discussion of this point, see Hu et al., 2006). In this application, we removed all information about the lowest frequencies in the signal by setting all values in $cA_n$ to zeros. This has the effect of a high-pass filter after reconstructing the signal.

This dampening or zeroing of approximation coefficients is sometimes referred to as "wavelet de-noising" in the signal processing literature.

One cannot directly specify the cutoff frequency for the wavelet filter. Instead, one chooses a level of decomposition $n$ which implicitly defines a high-pass bound. The approximation coefficients always contain the lowest frequencies in the signal, up to some frequency $f_c$. The cutoff frequency of the wavelet filter is then $f_c$, since it is the highest frequency not to be contained in the final reconstructed signal. The cutoff frequency is found to be

$$f_c = \text{Nyquist Frequency} / 2^n$$

where $n$ is the level of decomposition and the Nyquist frequency is equal to half the data sampling rate. Although we did not do this, in practice one could resample the signal before WMLDR to yield a specified cutoff frequency.

Using the Daubechies 4 wavelet, we performed an $n$ = 6 level decomposition, which passes frequencies above 244 Hz given a sampling rate of 31250 Hz. We chose this level after comparison of the signal-to-noise ratio (SNR) of spikes and reconstruction quality across various levels (Fig. 3B). Although an n = 7 level decomposition provides better clustering quality and less waveform distortion, using an n = 6 wavelet filter grants a much higher SNR with small losses in clustering ability (Fig. 4). We chose to compare our wavelet filter to a 4-pole Butterworth filter with a passband of 300-6000 Hz, since this is one of the most common settings of hardware filters, and one of the highest performing, with respect to waveform distortion, SNR, and clustering quality (Fig. 4). Using 244 Hz as the Butterworth high-pass cutoff marginally decreases signal distortion by minimally smearing the artificial "hump" across time (Fig. 3A, B),

but at the cost of further decreasing the SNR (not shown). Overall, the difference between 244Hz and 300Hz is not large enough to be relevant here.

*The Wavelet Filter Algorithm*

Pick a maximum decomposition level, $n$. Pick a wavelet and its associated decomposition and reconstruction filters (Fig. 1C & D). High-pass and low-pass decomposition filters are abbreviated as *HiD* and *LoD*, respectively. The corresponding reconstruction filters (which are the time inverses of the decomposition filters) are labeled as *HiR* and *LoR*. Then, for a signal *S*,

1. *Decomposition of the signal*.

Repeat for each $i = \{1, 2, ..., n\}$

- Convolve *S* with *HiD*. Keep only the even-indexed elements. Call this $cD_i$ and save.
- Convolve *S* with *LoD*. Keep only the even-indexed elements. Call this $cA_i$, but do not save unless $i = n$. Set this to be *S*.

*2. Reconstruction of the signal*.

- Set all coefficients in $cA_n$ to 0.
- Initialize $Sf = cA_n$.

Repeat for each $i = \{n, n - 1, ..., 1\}$,

- Upsample (Add zeros as even-indexed elements into $S_f$ and $cD_i$).
- Convolve *Sf* with *LoR*. Call this $cA^*$.
- Convolve cD*i* and *HiR*. Call this $cD^*$.
- $S_f = cA^* + cD^*$

*Cluster Quality*

To quantify clustering quality, we used two measures as described by Schmitzer-Torbert et al. (2005). *Isolation Distance* is a measure of how well-separated a cluster is from the rest of a data set and $L_{Ratio}$ indicates the distribution of non-cluster spikes around a cluster.

The Isolation Distance for cluster *c,* containing $n_c$ spikes, is defined as the squared Mahalanobis distance of the $n_c$th closest non-*c* spike to the center of *c.* The squared Mahalanobis distance is calculated as

$$D_{i,c}^2 = (x_i - \mu_c)^T \sum_C^{-1} (x_i - \mu_c)$$

where $x_i$ is the vector containing features for spike *i* (3 PCA coefficients per tetrode wire), and $\mu_c$ is the mean feature vector for cluster *c*. $\sum_c$ is the covariance matrix of spikes in cluster *c*. The Isolation Distance is not defined when $n_c$ is greater than the number of non-cluster spikes. A higher value indicates that non-cluster spikes are located farther away. The Mahalanobis distance (Mahalanobis, 1936) is used because it helps compensate for ellipse-shaped distributions of spikes, i.e. a point at any edge of an ellipse is equidistant from the center of the ellipse using Mahalanobis distance. Note that Isolation Distance is not normalized against cluster size, so that clusters with a large number of spikes will tend to have a higher Isolation Distance.

$L_{Ratio}$ is calculated as follows for cluster *c*:

$$L(c) = \sum_{i \notin c} 1 - CDF_{X^2_{df}}(D_{i,c}^2)$$

where $D_{i,c}^2$ is the squared Mahalanobis distance between non-*c* spike *i* and the center of *c* and $CDF_{X^2_{df}}$ is the chi-squared cumulative distribution function describing the distribution of spikes in

cluster *c*. The number of degrees of freedom is equal to the number of features used in the cluster space (here we use 3 principal components for each wire in a tetrode, df = 12). Then,

$$L_{Ratio}(c) = \frac{L(c)}{n_c}$$

A low $L_{Ratio}$ indicates that there is a relatively empty space between the cluster and other spikes in the data set. $L_{Ratio}$ positively correlates with Type II errors (false omissions) and Isolation Distance negatively correlates with Type I errors (false positives; Schmitzer-Torbert et al., 2005). Therefore, a lower $L_{Ratio}$ and a higher Isolation Distance together indicate better cluster quality. We tested for a significant difference between the clustering performance for the wavelet- and Butterworth-filtered spikes using the paired Student's t-test. The number of points on which PCA was performed was varied as a *window size*, centered on the spike peak. To assess a possible improvement in spike detection, we calculated the SNR for each neuron. We defined the SNR as the peak amplitude of a neuron's average filtered waveform divided by the standard deviation of the entire filtered recording session from which the spikes were extracted. The standard deviation was calculated using 60 1-second evenly distributed samples of the filtered data.

## Results

As found in non-neural applications, WMLDR is an effective means of removing the lower frequencies from an electrophysiological signal (Fig. 2), as a preprocessing step before spike detection and sorting. To assess the distortion of waveforms produced by different filtering techniques, we first assigned spikes to single-units using standard Butterworth bandpass filtering (4-pole, 300-6000Hz passband), detection via constant threshold, and manual clustering. From

these time-stamps, we then re-extracted spike waveforms from continuous data – either the original wideband signal (i.e. we took a spike-triggered average of the "raw" voltages) the wavelet-filtered, or the Butterworth-filtered signal. For neurons with the most common waveform shapes , typical of projection neurons in striatum (Fig. 3Bi, ii; Berke et al 2004) and hippocampus (Fig. 3Biii, iv), Butterworth filtering produces a highly distorted "valley" shape, while wavelet-filtered signals retain higher fidelity to the original wide-band signal. For briefer waveforms that represent likely interneurons, (e.g. Fig. 3Bv, vi) the distortion produced by Butterworth filtering was less marked but still typically more pronounced than with wavelet filtering. In no case did we observe marked distortion produced by wavelet filtering, although there was a slight tendency to produce a lowering of the signal around the spike peak; the extent of this effect varied with choice of wavelet decomposition level (Fig. 3C).

We noticed that part of the distorting effect of Butterworth filtering was to reduce the peak height of striatal and hippocampal projection neuron spikes (e.g. Fig. 2). We compared the signal-to-noise ratio (SNR) for presumed rat and mouse projection neurons (n=47), and found that wavelet filtering produced a significant increase in SNR over Butterworth filtering ($p < 0.05$, paired t-test). For cells with briefer waveforms (including presumed striatal and hippocampal fast-spiking interneurons), the overall difference in SNR was not significant n=19; $p = 0.486$, paired t-test), and a few cases even had higher SNR with Butterworth filtering. This is because Butterworth filtering generally shifts the spike signal towards zero mean, which brings the signal closer to an upper threshold for cells with large downward deflections (Fig. 3v, vi). Applying both a positive- and negative-threshold would remove this advantage over wavelet filtering.

The increased SNR observed for striatal and hippocampal projection neurons with wavelet filtering noticeably enhanced cluster separation, when plotting peak height on each wire (for example, see Fig. 4). To quantitatively assess this difference between filtering methods on spike discriminability, we performed principal components analysis (PCA) on spike waveforms, using varying sizes of time window centered on the spike peak. We then measured the extent of cluster separation using Isolation Distance and $L_{ratio}$ in principal components space as a function of window size (Fig. 5). The best results were obtained using narrow windows around the peak (~350-400μs), with wavelet filtering. This is a useful result for spike sorting, because it indicates that only a narrow window around the spike peak need be extracted for effective cluster discrimination in PCA space.

We quantified filter performance for a variety of filter types and parameters (Fig. 6), including both high- and band-pass Butterworth filters, higher-order versions of each, and an alternative IIR filter (Bessel bandpass). SNR determines the detectability of a spike using a constant threshold. An n=6 level wavelet filter outperforms all Butterworth filter types here, although the Bessel filter performs equivalently. The wavelet filter demonstrates markedly lower waveform distortion than any non-wavelet filter examined. The clustering performance of the wavelet filter, measured by Isolation Distance, was also significantly higher than the alternatives. In choosing a wavelet order, there is a tradeoff between SNR for initial detection and subsequent clustering performance. Although a level 6 wavelet filter has the most balanced performance, at some computational cost one could obtain even better results by using a level 5 wavelet-filter to detect spikes, then clustering them using either unfiltered waveforms or those obtained with a

level 7 wavelet-filter. Our results also show among IIR filters, using a Bessel filter is a far better option than regular Butterworth filtering.

WMLDR is an established algorithm that is computationally efficient (Mallat, 1989). For a signal of length $N$ and a high and low-pass filter set each of length $K$, the total decomposition and reconstruction of the signal requires at most $2KN$ multiplications and additions (Mallat, 1999), resulting in an operation that scales linearly with signal length. In our experience, using regular desktop computers, the execution time is comparable to Butterworth filtering and much less than the duration of the signal being processed even for recordings with >80 simultaneously processed channels. Thus,wavelet filtering is clearly fast enough to be used online for those laboratories that either do not wish to save the full high-speed wide-band signal, or that perform real-time spike sorting (e.g. for brain-machine interfaces).

## Discussion

We have shown several advantages for using wavelet filtering with electrophysiological data, compared to current standard methods. WMLDR can faithfully preserve spike shape, which is a useful partial indicator of neuronal phenotype. For striatal and hippocampal projection neurons, which make up the great majority of neurons in those regions, wavelet filtered spikes exhibit a significantly higher SNR, allowing for easier spike detection and enhanced spike discrimination through cluster analysis. The technique is based on relatively simple operations, and so is fast enough to be applied online. It is thus reasonable to use it as a pre-processing filter before standard threshold-based spike detection methods, which require a signal with the low frequencies removed. Alternatively, methods that use wavelet coefficients for spike detection (e.g. Nenadic and Burdick, 2005**,** Hulata et al. 2002) could modify this approach to avoid

redundant computation, by performing wavelet decomposition once for both removal of low frequencies and spike detection.

There is room for further refinements of the technique to increase the flexibility of the passband. First, a more subtle wavelet denoising technique might be used. In this paper we destroyed *all* the approximation coefficients, and, by not computing higher-level, lower-frequency detail coefficients, we effectively destroyed them as well. Second, we might employ a more complex wavelet algorithm called wavelet packet decomposition, along the lines of Hu et al., 2006. This is a more computationally intensive alteration of WMLDR can split both the high- and low-frequency components of a signal into equally-spaced frequency bands. WMLDR, by contrast, only splits the low-frequency components of a signal. This would enable the construction of a wavelet band-pass filter with arbitrarily precise control over the passband, although with a higher computational cost than our current approach.

## References

Addison P. The Illustrated Wavelet Transform Handbook: Introductory Theory and Applications in Science, Engineering, Medicine. Institute of Physics Publishing:London, 2002.

Adeli H, Zhou Z, Dadmehr N. Analysis of EEG records in an epileptic patient using wavelet transform. J. Neurosci. Methods, 2003; 123: 69-87.

Barthó P, HIrase H, Monconduit L, Zugaro M, Harris K, Buzsáki G. Characterization of Neocortical Principal Cells and Interneurons by Network Interactions and Extracellular Features. J. Neurophysiol., 2004; 92: 600-8.

Berke J, Okatan M, Skurski J, Eichenbaum H. Oscillatory Entrainment of Striatal Neurons in Freely Moving Rats. Neuron, 2004; 43(6): 883-96.

Berke J, Hetrick V, Breck J, Greene R. Transient 23-30Hz oscillations in mouse hippocampus during exploration of novel environments. Hippocampus, in press.

Berkes P, Wilbert N, Zito T. Modular toolkit for data processing (version 2.2). http://mdp-toolkit.sourceforge.net.

Butterworth S. On the Theory of Filter Amplifiers. Wireless Engineer, 1930; 7:536-41.

Cesar, RM Jr, Costa LF. Neural cell classification by Wavelets and multiscale curvature. Biol. Cybern., 1998;79:347-360.

Clarençon D, Renaudin M, Gourmelon P, Kerckhoeve A, Catérini R, Bolvin E, Ellis P, Hille B, Fatôme M. Real-time spike detection in EEG signals using the wavelet transform and a dedicated digital signal processor card. J. Neurosci. Methods, 1996; 70: 1: 5-14.

Csicsvari J, Hirase H, Czurko A, Buzsáki G. Reliability and State Dependence of Pyramidal Cell–Interneuron Synapses in the Hippocampus: an Ensemble Approach in the Behaving Rat. Neuron, 1998;21:179-89.

Daubechies I. Orthonormal Bases of Compactly Supported Wavelets. Comm. Pure Appl. Math., 1988;41:909-996.

Daubechies I. Ten Lectures on Wavelets. SIAM: Philadelphia, 1992.

Hu X-G, Liu, L-T, Hinderer J, Hsu, HT, Sun, H-P. Wavelet filter analysis of atmospheric pressure effects in the long-period seismic mode band. Phys. Earth Planet. Int. 2006, 154: 70-84.

Hulata E, Segev R, Ben-Jacob E. A method for spike sorting and detection based on wavelet packets and Shannon's mutual information. J. Neurosci. Methods, 2002; 117:1-12.

Letelier JC, Weber PP. Spike sorting based on discrete wavelet transform coefficients. J. Neurosci. Methods, 2000; 101: 93-106.

Lewicki M. A review of methods for spike sorting: the detection and classification of neural action potentials. Network: Computation in Neural Systems, 1998; 9: R53-R78.

Mahalanobis P. On the generalized distance in statistics. Proc. Natl. Institute of Science of India, 1936;12:49-55

Mallat S. Multifrequency channel decompositions of images and wavelet models. IEEE Trans. Acoust. Speech Signal Processing. 1989; 37:2091-2110.

Mallat S. A Wavelet Tour of Signal Processing, 2nd edition. Academic Press, 1999.

Markazi SA, Qazi S, Stergioulas LS, Ramchurn A, Bunce D. Wavelet Filtering of the P300 Component in Event-Related Potentials. Engineering in Medicine and Biology Society, EMBS '06. 28th Annual International Conference of the IEEE, 2006:1719-22

Misiti M, Misiti Y, Oppenheim G, Poggi JM. Wavelet Toolbox for Use with Matlab. Mathworks, 2000.

Nenadic Z, Burdick JW. Spike detection using the continuous wavelet transform. IEEE Trans. Biomed. Engin., 2005;52:74-87.

Oliphant T. NumPy: Numerical Python. http://numpy.scipy.org, 2006

Plexon Inc. Offline Sorter. 2003. Dallas, TX.

Quiroga RQ, Nadasdy Z, Ben-Shaul Y. Unsupervised Spike Detection and Sorting with Wavelets and Superparamagnetic Clustering. Neural Computation, 2004;16:1661-1687.

Schmitzer-Torbert N, Jackson J, Henze D, Harris K, Redish AD. Quantitative Measures of Cluster Quality For Use in Extracellular Recordings. Neuroscience, 2005;131:1-11.

van Rossum G. Python Library Reference. CWI Report CS-R9524, 1995.

Valens C. A Really Friendly Guide to Wavelets, http://pagesperso-orange.fr/polyvalens/clemens/wavelets/wavelets.html.

Vetterli M, Herley C. Wavelets and filter banks: theory and design. IEEE Transactions on Signal Processing, 1992; 40: 2207-32.

Wasilewski F. PyWavelets. Discrete Wavelet Transform in Python. http://www.pybytes.com/pywavelets, 2006

## Tables

Table 1. Frequency content of detail and approximation coefficients at wavelet decomposition levels 1-6, for a signal sampled at 31250Hz.

| *Coefficients* | *Frequency content* |
|---|---|
| cD1 | 7812 - 15625 Hz |
| cD2 | 3906 - 7812 Hz |
| cD3 | 1953 - 3906 Hz |
| cD4 | 976 - 1953 Hz |
| cD5 | 488 - 976 Hz |
| cD6 | 244 - 488 Hz |
| cA6 | 0 - 244 Hz |

## Figure Captions

Figure 1. Schematic description of the wavelet-filtering algorithm. $cA_i$ denotes approximation coefficients at level *i*, $cD_i$ denotes detail coefficients at level *i. A*. Block-diagram representation of the decomposition stage of the wavelet filtering algorithm (see Methods). *B.* Representation of the reconstruction phase. *C*. The decomposition wavelet filters. The high-pass filter is in black

labeled as HiD, the low-pass filter is in grey labeled as LoD, and each has 8 coefficients. The y-axis represents coefficient values. *D*. The reconstruction wavelet filters. The high-pass filter is in black labeled as HiR, and the low-pass filter is in grey labeled as LoR.

Figure 2. Comparison of unfiltered (top), wavelet filtered (middle, level 6 decomposition) and Butterworth filtered (bottom, 300-6000 Hz bandpass) traces from the same section of continuously recorded striatal tetrode data. Dotted black lines represent a threshold of 4 times the standard deviation calculated across the whole recording session.

Figure 3. Demonstration of the distortions caused by wavelet and Butterworth filtering. *A*. Filtering of a 1 ms Hanning window, to illustrate the general type of distortion caused by each filtering method. *B*. Average spike waveforms for 6 representative cells. Solid black traces are wavelet filtered (level 6 decomposition), solid grey traces are Butterworth filtered (300-6000 Hz $4^{th}$ order bandpass), and dotted black are unfiltered. Each set of spikes is normalized such that the largest spike has height 1 for the purpose of comparing relative shapes. The SNR is indicated by black text on top for wavelet-filtered cells, and grey text on bottom for Butterworth-filtered cells. Fast, sharp waveforms generally benefit in SNR from wavelet-filtering, however, the more common, "wider" waveform shapes have consistently higher SNR when wavelet-filtered. *C*. Average waveform shape of one cell, wavelet filtered with different levels of decomposition. Note that level 7 gives a near-perfect reconstruction of the unfiltered spike shape, but passes frequencies above 122 Hz, which reduces SNR during spike extraction. In our analysis, we used

level 6, which has a cutoff frequency of 244 Hz and a much improved SNR over level 7, while better preserving spike shape than level 5 (Fig. 6).

Figure 4. Comparison of cluster separation for wavelet- and Butterworth-filtered spikes. In this example, five cells were recorded simultaneously from a striatal tetrode. *Left:* The average waveform for each cell on each wire of the tetrode (1 ms per wire). Blue and red traces are presumed fast-spiking interneurons, while others are medium spiny neurons (MSNs). *Middle*: Isolation Distance of wavelet (W) and Butterworth (B) filtered spikes, calculated using only the peak heights on each tetrode wire. *Right*: plot of peak heights for each cluster, showing visibly improved separation using wavelet filtering.

Figure 5. Wavelet filtering allows superior cluster separation with fewer data points. To determine how much of the spike waveform contributes to clustering performance, PCA was performed with varying window sizes (see Methods). *Top*: Plot of Isolation Distance versus window size used to perform PCA. Larger values of Isolation Distance are better. Circles are data from wavelet filtered clusters, and triangles are Butterworth filtered. A total of 47 presumed projection cells (30 from rat striatum, 17 from mouse hippocampus) across 7 tetrodes over 2 sessions each were used to compute cluster quality. Crosses above the data points indicate that there was a significant difference between the two filtering methods ($p < 0.05$, paired t-test, without correction for multiple comparisons). *Middle*: Plot of $L_{Ratio}$ versus the window size. Lower values of $L_{Ratio}$ are better. For both measures, the best performance was obtained using wavelet filtering using a ~350-400 μs window, corresponding to approximately 11-13 samples at

31250Hz. *Bottom*: a visual representation of the time window used for PCA superimposed of an example mean cell waveform (wavelet-filtered in black, Butterworth-filtered in grey).

Figure 6. Quantitative comparison of different filtering methods. *Left:* The SNR (see Methods) determines spike detectability. *Middle:* Waveform distortion is calculated as the mean squared Euclidean distance between each cell's mean unfiltered waveform and mean filtered waveform (n=47 projection cells). The waveforms are normalized such that the unfiltered waveform has peak height 1. The Isolation Distance (see Methods) is calculated using 3 PCA coefficients per wire (on 4 wires) performed on a 400μs window of the spike, centered on the peak.

Figures

Figure 1.

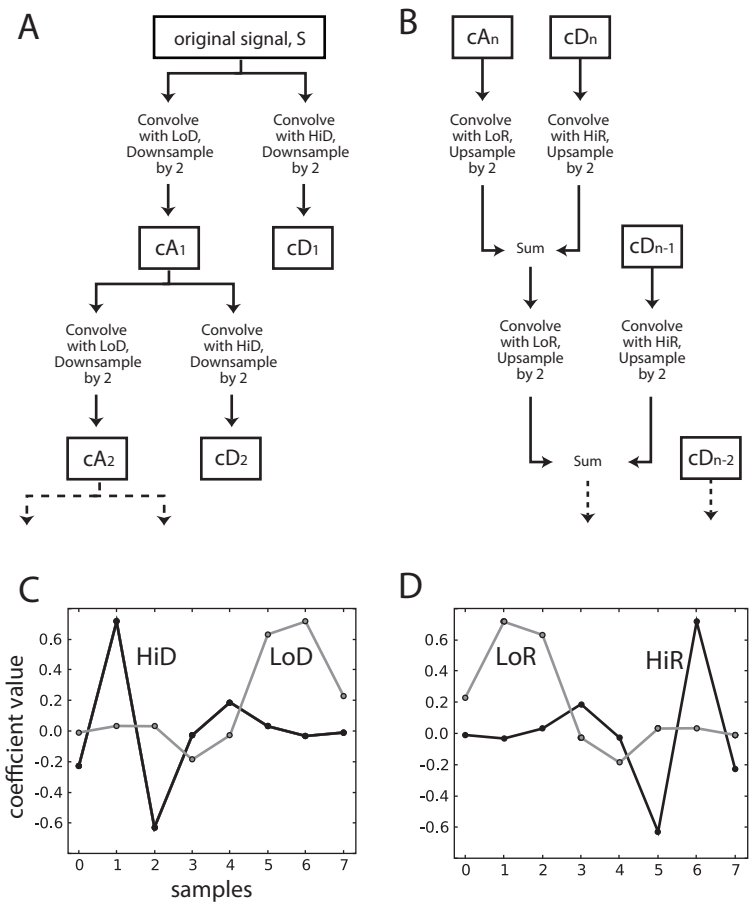
A
original signal, S
Convolve with LoD, Downsample by 2
Convolve with HiD, Downsample by 2
cA1
cD1
Convolve with LoD, Downsample by 2
Convolve with HiD, Downsample by 2
cA2
cD2
B
cAn
cDn
Convolve with LoR, Upsample by 2
Convolve with HiR, Upsample by 2
Sum
cDn-1
Convolve with LoR, Upsample by 2
Convolve with HiR, Upsample by 2
Sum
cDn-2
C
HiD
LoD
coefficient value
samples
D
LoR
HiR

Figure 2.

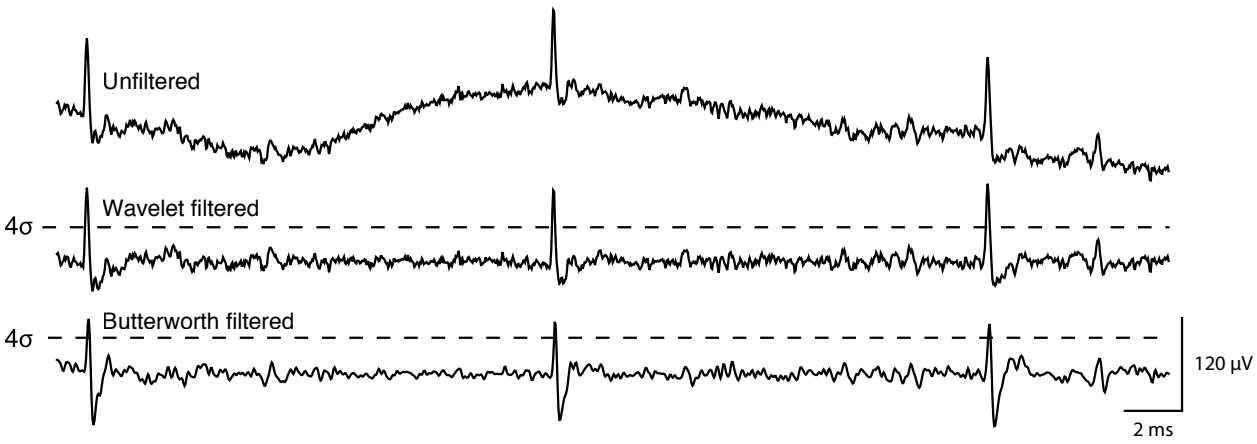


Figure 3.

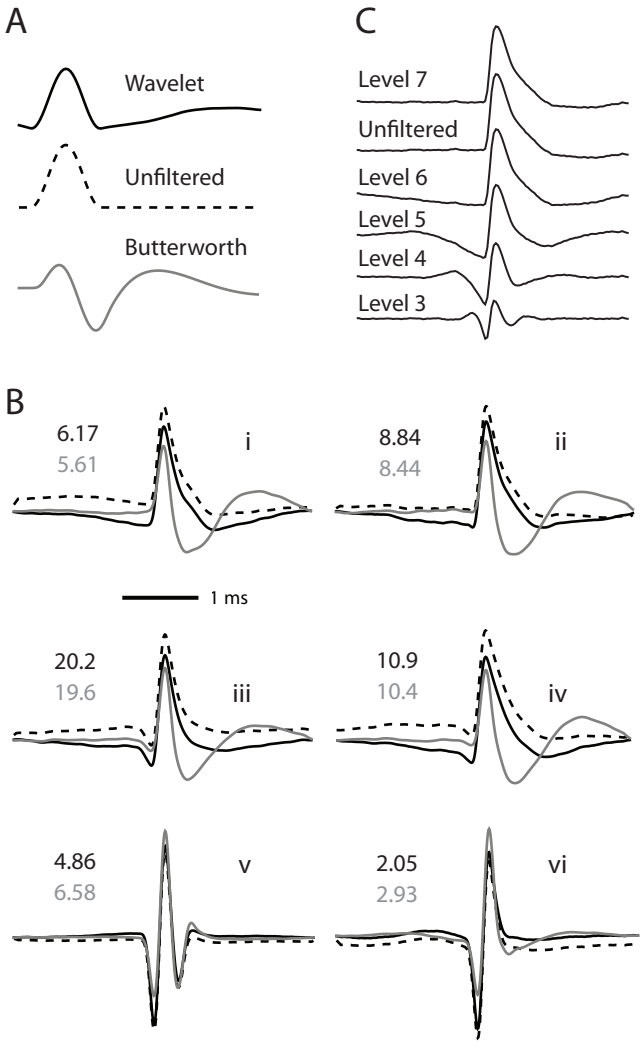

Figure 4.

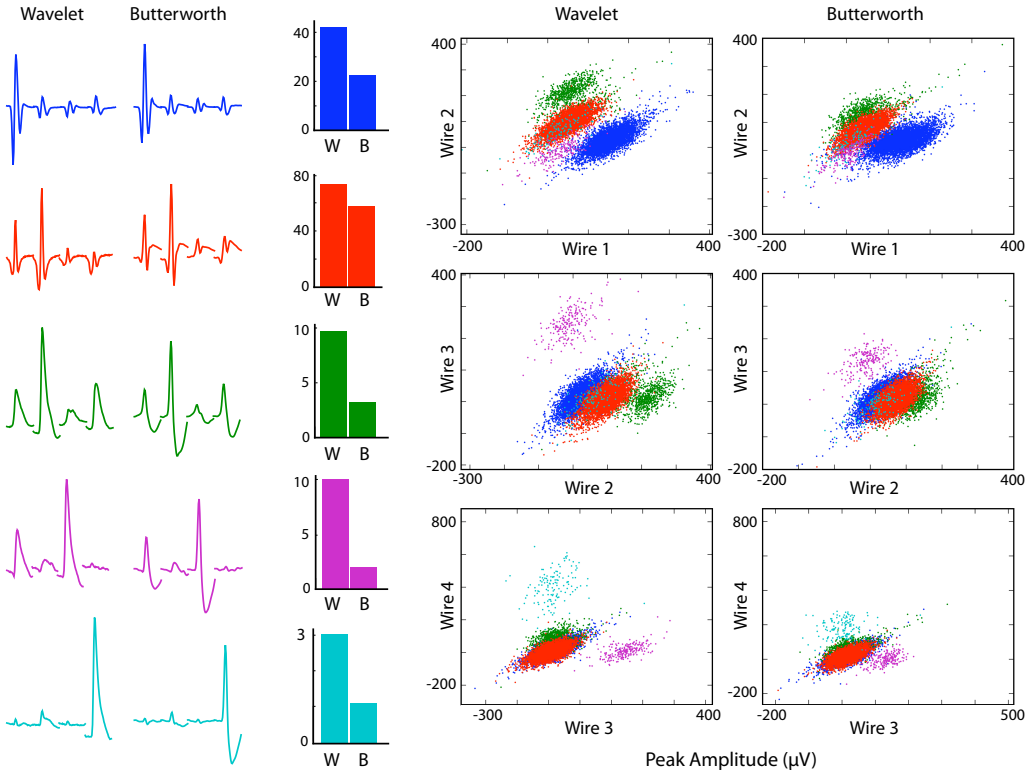
Wavelet
Butterworth
W B
Wire 1
Wire 2
Wire 3
Wire 4
Peak Amplitude (μV)

Figure 5.

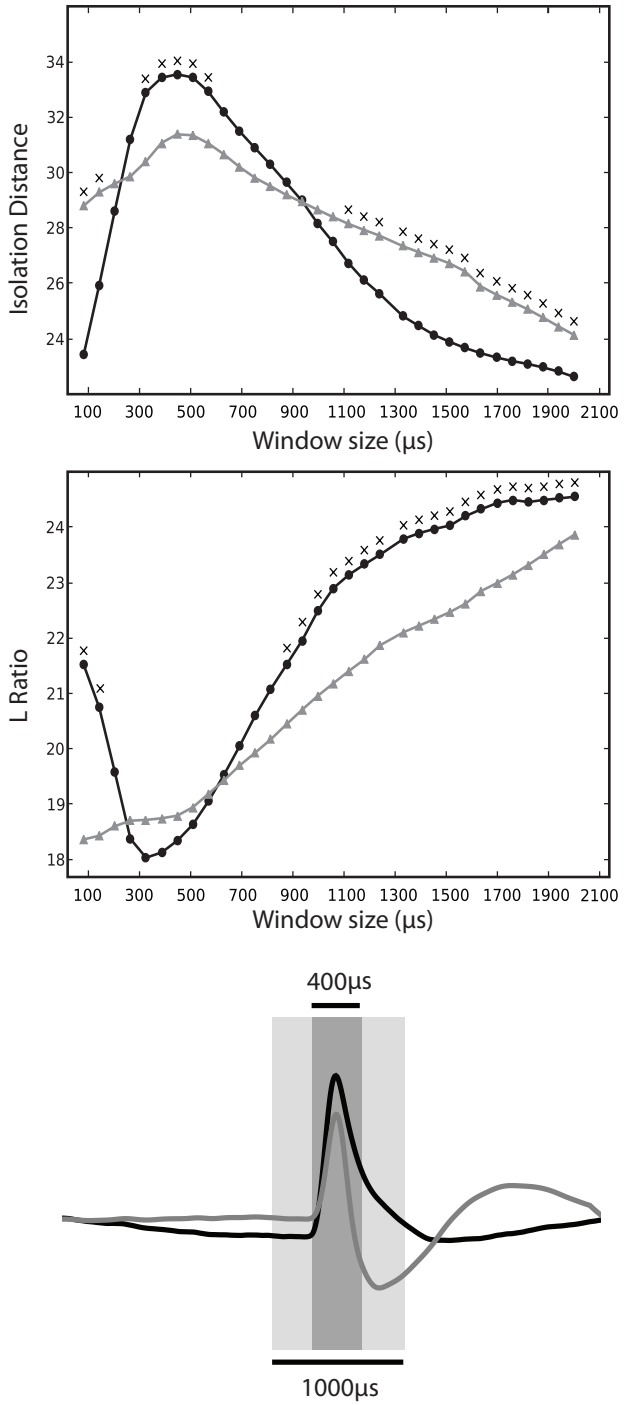
Isolation Distance
34
32
30
28
26
24
100 300 500 700 900 1100 1300 1500 1700 1900 2100
Window size (µs)
L Ratio
24
23
22
21
20
19
18
100 300 500 700 900 1100 1300 1500 1700 1900 2100
Window size (µs)
400µs
1000µs

Figure 6.

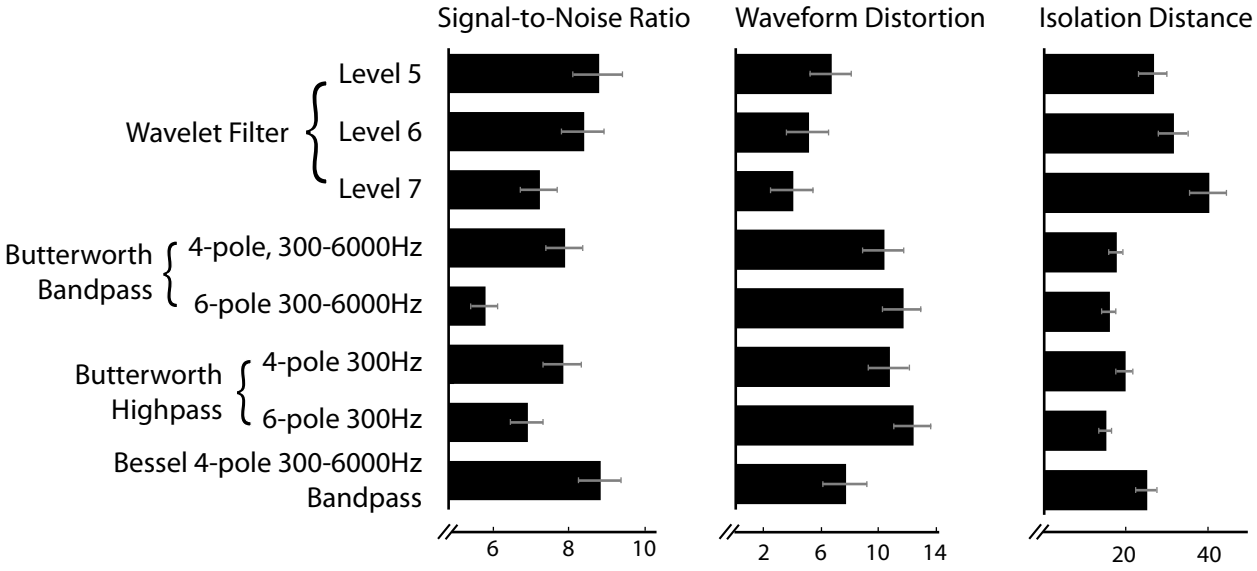
Signal-to-Noise Ratio
Waveform Distortion
Isolation Distance
Wavelet Filter
Level 5
Level 6
Level 7
Butterworth Bandpass
4-pole, 300-6000Hz
6-pole 300-6000Hz
Butterworth Highpass
4-pole 300Hz
6-pole 300Hz
Bessel 4-pole 300-6000Hz Bandpass
6
8
10
2
6
10
14
20
40

# Chapter 2: Opposing Effects of Amphetamine and Eticlopride on Striatal Fast-Spiking Interneuron Firing Rate

In every organism, there exists a dynamic mass of unmade decisions. At every moment, some of these decisions are chosen to be enacted, while others are suppressed. In mammals, a group of subcortical nuclei known collectively as the basal ganglia play a vital role in the refinement and selection of these unrealized decisions (Mink 1996; Murer et al., 2002; Graybiel et al., 2004). The dysfunction these nuclei likely contributes to neurological diseases such as Parkinson's disease, obsessive-compulsive disorder, drug addiction and Tourette's syndrome (Albin et al., 1989; Cummings, 1993; Berke and Hyman, 2000; Leckman et al., 2006).

## *The Basal Ganglia*

The basal ganglia span the midbrain, diencephalon and forebrain, and are positioned dorsal to the brainstem. They are heavily interconnected and have extensive outputs to the thalamus and from cerebral cortex. The cortex provides the main source of input to the basal ganglia, synapsing mostly in the striatum. The striatum is the largest nucleus of the basal ganglia and serves as the input component and first information processing step. The output of the striatum exclusively reaches other nuclei of the basal ganglia, primarily the globus pallidus and substantia nigra. The striatum may be divided in several different manners, despite its homogenous appearance in simple histology in the rat. The most straightforward division is into dorsal and ventral regions. The dorsal striatum is composed of two nuclei, the caudate nucleus and the putamen. The ventral striatum contains the ventral portions of the caudate and putamen, as well as the nucleus accumbens (Gerfen and Wilson, 1996). One can also divide the striatum topographically into three regions based on the type of input it receives from cortex: the

sensorimotor, limbic, and associative striatal regions. Sensorimotor striatum receives motor, premotor and somatosensory cortical afferents in dorsolateral striatum. Ventromedial striatum has connections from limbic areas such as the hippocampus, prelimibic and infralimibic cortices and the amygdala. This area also includes the nucleus accumbens. Temporal, prefrontal and parietal areas innervate the associative striatal cell population, located in between the sensorimotor and limbic regions (Nakano et al., 2000, Voorn et al., 2004).

On a smaller scale, the striatum is a neurochemical mosaic, composed of "patches" and "matrix." These unevenly distributed regions are identified by the molecules that cells express within their boundaries. The patches are identified mainly by high expression of μ-opioid receptors and receive limbic inputs. The matrix characteristically has high acetylcholinesterase activity and is innervated by motor and sensory cortex (Gerfen, 1984). Dorsolateral striatum has a higher density of matrix areas than medial striatum, whereas ventral striatum is denser in patches (Herkenham and Pert, 1981).

*Striatal Cell Types*

The patch-matrix regions provide boundaries restricting dendritic fields of the GABAergic medium-spiny neurons (MSNs), the most prevalent cell type of the striatum which composes at least 90% of the region's cell population (Graveland et al., 1985). The MSNs support the bulk of information processing in the striatum. They receive extensive innervation from cortical axons, but their firing patterns are significantly shaped by striatal interneurons (Mallet et al., 2005). There are four known striatal interneuron types: three GABAergic and one cholinergic. The best understood class of GABAergic interneuron is the fast-spiking interneuron (FSI), which sends axons freely over the patch-matrix boundaries and is perhaps the most

powerful source of local inhibition in the striatum (Tepper et al., 2004). These cells contain the calcium-binding compound parvalbumin (historically, their defining feature) and are coupled electrically by gap-junctions. The exact role of FSIs in striatal computation is unknown, but they provide reliable and powerful perisomatic inhibition of MSNs, strongly affecting the occurrence and timing of MSN action potentials (Kawaguchi, 1993, 1997; Koos and Tepper, 1999). Although MSNs themselves have inhibitory connections to each other, the strength of these synapses are extremely weak compared to FSI inhibition (Czubayko & Plenz 2002; Tunstall et al., 2002; Plenz, 2003).

FSIs are more excitable than MSNs, and so tend to fire sooner after a burst of cortical input (Mallet et al., 2005). In order for an MSN to successfully fire an action potential, it must avoid FSI inhibition by either firing in a window where FSIs are silent, or overcoming inhibition by coincident cortical input. This feedforward inhibition may serve to increase contrast in the striatum by suppressing weakly activated MSNs, leaving only strongly selected (and presumably appropriate) actions represented in the striatum.

In a post-mortem analysis of individuals with severe Tourette's syndrome, FSIs were conspicuously less numerous in the striatum compared to healthy controls (Kalanithi et al., 2005). Leckman and colleagues (2006) suggested that this deficit of FSIs in the striatum would lead to a reduced ability to suppress and filter out less-salient details from consciousness, manifesting physically as the tics that characterize Tourette’s syndrome.

Many psychoactive drugs alter normal dopamine transmission. A therapy to reduce tic severity and frequency in Tourette’s remains treatment with classical antipsychotic drugs (major tranquilizers) that are dopamine D2 receptor antagonists. The striatum has the highest density of

dopamine receptors in the rat brain (Boyson et al., 1986; Weiner et al., 1990) and thus is a major site of action for psychoactive drugs. There are two main subtypes of dopamine receptor, and each have differing effects on cells. Activation of D1 receptors tend to excite cells, whereas D2 receptor activation is generally inhibitory. So, given that the striatum is a target for drug action modulating dopamine, it is important to know how striatal FSIs are affected by psychoactive drugs, particularly psychostimulants and antipsychotics.

*Predicted Firing Rate Changes*

There has been no published study to our knowledge exploring pharmacological modulation of FSIs in awake animals. Here, we examine the changes in firing patterns of FSIs after giving either the antipsychotic eticlopride or the psychostimulant amphetamine. Eticlopride is a potent dopamine D2-receptor antagonist that induces sedation without catalepsy (Ferrari and Giuliani, 1995). Amphetamine is a psychostimulant that increases synaptic dopamine concentration through and at high doses can induce tic-like stereotypies that impair the normal variety of behavior.

Do psychostimulants and antipsychotics affect locomotion and stereotypy by specifically affecting FSIs? One hypothesized role of the FSI population in the striatum has been that of a global feed-forward inhibition network in the striatum acting to specifically suppress unwanted locomotor behavior. The striatum is involved in generating locomotor behavior, so we may make some simple predictions about FSI firing rate changes after drug administration. Under the global feed-forward behavior inhibition hypothesis, we expect FSIs to decrease their firing rate during the hyperkinesia induced by amphetamine. Since the rat is more behaviorally active at that time, we expect striatal inhibition to be lax. Then, eticlopride administration would increase FSI firing

rates, an effect which would help offset the low numbers of FSIs in the Tourette's-affected striatum. So, based on a simple conception of FSIs as a source of global feedforward inhibition in the striatum, we expect to see opposing changes in firing rate, with amphetamine decreasing FSI firing rate and eticlopride increasing it.

FSIs and MSNs can be identified by their extracellular waveform (Fig. 1), so their activity can be recorded from awake, freely moving animals (Berke et al., 2004). Effectively distinguishing these cells is made possible by the new filtering technique described in Chapter 1 of this thesis. We recorded single-unit activity from the striatum after an amphetamine or eticlopride injection and observed opposing changes in FSI firing rate between the two drug treatments in directions contrary to our hypothesis. This effect was not mirrored as robustly by the MSN population.

## Method

### *Electrophysiology*

Two Long Evans rats were used. Experiments were performed during the light period of a 12:12 light/dark housing cycle. Rats were implanted with a 21-probe drive, with 21 independently lowerable probes, of which 18 are tetrodes and 3 are stereotrodes. Metal alloy wires were twisted together in groups of four or two to form tetrodes or stereotrodes. Their tips were electroplated with non-cyanide gold to lower impedances. The drive was implanted above the right striatum, with 18 probes targeting the caudate-putamen, and 3 targeting the nucleus accumbens. Skull screws were implanted in contact with the dura mater as a recording reference. Following implantation, probes were lowered to their target location over the course of a week, moving greater than 0.3 mm per day for the first week. Once target locations were reached,

probes were not moved more than 0.04 mm per day, to not disturb surrounding tissue and maintain stable recordings once FSIs were located. Probes were monitored on a 4-channel oscilloscope, and were checked daily for putative FSIs, identified by their firing pattern and sharp waveform shape. Once a possible FSI was found on a tetrode, it was not moved for as many days as the cell remained stable. When a sufficient amount of FSIs were stable across all tetrodes, the drug treatment protocol was begun. When recording single units, a wideband signal (filtered 1-9000Hz hardware bandpass) was continually digitized during at 31250 Hz using an 81-channel system built around custom amplifiers (Boston University Electronics Design Facility) and custom LabView data acquisition software. Digital video was recorded with the same system for one rat.

*Treatment*

Rats were allowed a 1-week recovery period after surgery during which tetrodes were lowered to target locations and the rat was acclimated to the recording environment. Drug treatment began once enough FSIs were stable across all probes. Four unique drug treatments were given for each rat, administered IP, never exceeding 0.5 mL per injection. For the first rat, the order of treatment is as follows: Day 1, “High Amphetamine,” 2.5 mg/kg. Day 2, “High Eticlopride,” 1.0 mg/kg. Day 3 “Low Amphetamine,” 0.5 mg/kg. Day 4, “Low Eticlopride,” 0.2 mg/kg. For the second rat, the high doses and low doses were swapped. However, analogous doses of amphetamine were still administered before eticlopride.

Each experiment was 3.5 hours long. Baseline activity was recorded, then a saline injection was given at 30 minutes. At 1.5 hours, a drug injection was given, and at 3.5 hours, the experiment ended. In all cases, injections with eticlopride induced sedation, and amphetamine

injection induced a hyperactive state. After the experiment period, the animal remained in the recording environment for less than 45 minutes while tetrodes with no FSIs were moved deeper. Rats were recorded for a maximum of 8 days after first drug treatment.

*Histology*

After the drug treatment protocol ended, tetrode locations were lesioned by injection of 20μA of current for 10 seconds through each probe wire. Rats were then perfused with 4% paraformaldehyde (PFA) to facilitate identification of tetrode lesions. The brain was removed after perfusion and stored in PFA for 24 hours, then moved to 30% sucrose in 1X PBS. Brains were frozen and sliced in a microtome at 20-40 μm and Nissl stained. Slices were imaged with a light microscope and camera, and exact final stereotaxic coordinates were found by mapping histology slice images onto the Paxinos & Watson brain atlas (5th edition ) using Sqirlz Morph software.

*Data Analysis*

The continuously digitized signal was wavelet-filtered (Wiltschko et al., 2008) to remove the LFP, and then spike detection was performed using a flat threshold on the smoothed nonlinear energy (calculated with a 400μs moving window) of the filtered signal (Mukhopadhyay and Ray, 1998). Detected waveforms were manually cluster-cut using OfflineSorter (Plexon Inc.), then their time stamps and waveforms were exported to Matlab through NeuroExplorer for further analysis. Units that were not stable across both injections were excluded.

Firing-rate analysis was performed by binning spikes into 1 minute windows, and then smoothing the time-series with a 3-point Gaussian kernel (Figure 2B). The firing rate time-series

was then analyzed by experiment block. The saline block began 10 minutes after saline injection, and ended right before the drug injection. The drug block began 10 minutes after drug injection, and lasted until the end of the recording session. All reported block firing rates are the median value of the firing rate time-series.

We did not use spikes that co-occurred with high-voltage spindles (HVSs). HVSs occur when the animal is stationary, but not asleep. Normally silent striatal cells will fire strongly during HVSs, and many cells (including FSIs) will drastically alter their firing pattern. The occurrence of HVSs after amphetamine is extremely rare, as the animal is constantly moving, whereas a rat sedated with eticlopride will exhibit more HVS than at baseline. We therefore identified the occurrence of HVSs by manually inspecting spectrograms for each session, and used sections of time within each block where no HVSs occurred.

To test for significant differences in firing rates between saline and drug blocks, the Mann-Whitney U Test was used. The time-series from the saline and drug blocks were tested for a significant difference for $p < 0.01$, with a post-hoc Bonferroni correction, where the number of samples was taken to be the length of the drug block in minutes.

## Results

### *Identifying Striatal Cell Types*

We made extracellular recordings in the striatum of three rats awake and freely moving rats. The data presented here is from two rats; analysis is ongoing for the third. The phenotype of single units in striatum can be inferred from the shape of their extracellular waveform. In accordance with previous studies (Berke et al., 2004), we used the waveform peak-width at half peak height, the peak-to-valley time and firing rate to classify units as either an FSI or an MSN

(Fig. 1). FSIs are characterized by narrow peak widths and short peak-to-valley times, with firing rates much higher than MSNs. We defined FSIs as having peak widths at half-maximum between 50 and 200μs, and peak-to-valley times between 100 and 455μs, with a minimum firing rate of 5 Hz. MSNs had considerably wider waveforms and lower firing rates. Cells were identified as MSNs if their peak-width was between 150 and 450μs and peak-to-valley times between 560μs and 1500μs. Firing rate was not used to select MSNs. Units that did not fit either criteria were left unidentified and not analyzed further in this study.

*Opposing Firing Rate Changes After Drug Injection*

Animals were given either eticlopride or amphetamine by IP injection at a high or low dose (see Method). The high and low doses for amphetamine are 2.5 and 0.5 mg/kg, respectively. For eticlopride, the high and low doses are 1.0 and 0.2 mg/kg. In this ongoing study, we have not yet extracted enough units from low doses to analyze them separately. Therefore, we have grouped both low and high doses together for each drug.

After drug injections, striatal cells changed their firing rates (Figure 2). In contradiction with our hypothesis, amphetamine tended to increase firing rates. 25 out of 32 FSIs significantly increased their median firing rate ($p < 0.01$) after amphetamine injection (Figure 3A). 17 out of 32 MSNs increased their firing rate after amphetamine as well (Figure 3C). The MSNs exhibited a smaller proportion of significantly increasing cells, and also showed a much higher fraction of cells that had no significant change. Interestingly, the FSIs that decreased rate or showed no significant change all had firing rates in the saline block less than 15 Hz, suggesting a possible frequency-dependent effect.

In response to eticlopride, 8 of 11 FSIs significantly decreased their firing rate, again in contradiction with our hypothesis. The MSN population had almost as many cells decrease as exhibit no change (13 showed no change, 12 decreased out of 27). Of all 43 FSIs, we recorded three over consecutive amphetamine and eticlopride days. All three exhibited the same opposing drug effects as the population.

Rebec and colleagues (e.g. Wang and Rebec, 1993) have segregated the MSN population into locomotor-coding and non-locomotor-coding MSNs and shown different responses to drug administration between the two. Locomotor-encoding cells tend to increase their firing for amphetamine, while the non-locomotor population do not. We did not do any such categorization for the MSNs. The FSI population does not require subdivision based on encoding to reveal a robust response to drug.

Overall, we found no clear relationship between location in striatum and drug effect for FSIs (Fig. 4A, B) or MSNs (Fig. 4C, D). The uneven spatial distribution of FSIs and MSNs in this data set prevents drawing meaningful links between striatal position and firing rate. However, we are in the progress of expanding the data set to include more cells sampled from ventral striatum.

## Discussion

Using a novel filtering method that preserves spike-shapes to aid in the identification of cells via their extracellular waveform (Wiltschko et al., 2008), we identified two phenotypically distinct striatal cell sub-populations. We then completed a simple analysis of their firing rate changes in response to systemic psychostimulant or antipsychotic treatment. Amphetamine generally increases FSI firing rate, while eticlopride decreases it. MSNs also demonstrate the

opposing firing rate changes seen in FSIs, but not nearly as consistently; overall, there are many more MSNs than FSIs that show no significant change or a change opposite to the majority.

*Prior Studies*

It has been shown previously that systemic amphetamine injection generally increases striatal cell firing rate (Haracz et al., 1989; Haracz et al., 1993; Wang and Rebec, 1993; Rebec et al., 1997; West et al., 1997; Kish et al., 1999). Some cells exhibit no change, while a small proportion of cells decrease their firing rate. Most effort in explaining the variety of response has focused on separating MSNs into motor-related and non-motor related cells. MSNs that fire preferentially during movement are more likely to be excited by amphetamine injections than non-motor related units. This follows naturally from the fact that amphetamine increases locomotion. Cells selectively firing during certain kinds of locomotion will obviously be more stimulated during amphetamine hyperkinesia. It is likely, however, that a some of the motor group of cells analyzed in the literature may be fast-spiking interneurons, or other interneuron types. Wang and Rebec (1993) report motor-related neurons with baseline firing rates greater than 10 Hz. Some of these high-firing units reach almost a 90 Hz firing rate after amphetamine, which is uncharacteristically high in the striatum for anything except an interneuron.

However, in the current study, we do not explicitly make any groupings based on cell firing preferences. The FSI population, identified principally by their extracellular waveform, naturally exhibit a robust firing rate change in response to amphetamine and eticlopride. Our data show the previously reported heterogeneity in MSN response to amphetamine, but we did not attempt to make sub-classifications based on motor or non-motor firing preferences. An overall suppression of firing rate has been seen in previous studies after dopamine depletion.

Costa and colleagues (2006) showed that roughly 80% of striatal cells in transgenic dopamine transporter knockout mice are depressed by AMPT-induced dopamine depletion. This effect was shown in opposition to cortex, where half of recorded cells increased, and half decreased firing rates. This study made no sub-groupings of cell by phenotype (interneuron or projection cell) or response type (motor or non-motor). Wang and Rebec (1993) found that amphetamine-induced excitation of single-units could be reversed by IP injection of haloperidol (an antipsychotic with nonspecific D1/D2 receptor antagonism).

To our knowledge, this is the first study examining the effects of eticlopride on single-unit activity in the striatum. We found that eticlopride generally decreased striatal cell firing. FSIs were more consistently and strongly inhibited as a population than MSNs. The MSN population was weakly inhibited by eticlopride, with more cells showing no significant change than a depression.

*FSI Behavior Does Not Align with a Global Feedforward Inhibition Model*

The global feedforward inhibition model of FSI function is only one of many possible ways to conceive of the role of FSIs in the striatum. Our hypothesis postulates that FSIs are exclusively activated during the suppression of unwanted behavior. So, during periods of hyperkinesia induced by amphetamine, we predicted that FSIs would reduce their firing to allow for increased behavioral expression. Conversely, during eticlopride sedation, we predicted that FSIs would increase their firing rate, due to their role in suppressing locomotion. Clearly, the hypothesis is an oversimplification, and even then, our results directly contradict it.

However, it remains certain that the role of the striatal FSI is to shape MSN firing dynamics, following from the fact that FSIs synapse almost exclusively onto MSNs. However,

the details of this shaping are not clear. Mallet et al. (2005) show that FSIs are able to exert direct inhibition of MSN firing. However, for all sessions where an FSI and MSN were simultaneously recorded on the same tetrode, we never found evidence of monosynaptic depression in their cross-correlogram (data not shown). A separate unpublished data set recording striatal cells during a behavioral task (Gage et al., in preparation) also lacked any such interaction in simultaneously recorded FSI-MSN cross-correlograms. Even though the specifics of FSI-MSN interactions are not fully elucidated, it is still of interest that FSIs are robustly affected as a population by clinically relevant drugs.

The effect might arise from changes in the cortical signal to FSIs, changes in activity within the basal ganglia, and also direct effects on FSI dopamine receptors. Within the basal ganglia, an important loop pathway affecting FSIs is the connection from the GP back onto striatal interneurons. However, increased striatal dopamine predicts a change in firing rates caused by the striatum-GP loop in the opposite direction than we observed. If amphetamine is present in the striatum, D2 MSNs would be suppressed via the inhibitory action of the DA D2 receptor, thus releasing the GP from inhibition. The GP would then inhibit FSIs, suppressing their firing. By the same logic, if eticlopride frees D2 MSNs from dopaminergic inhibition, we expect to see increased FSI firing rate as theoutcome. For both drugs, we saw the opposite result.

Finally, rough striatal location does not seem to explain the variety of effects on FSIs and MSNs. However, we did not examine whether a cell was in a patch or a matrix. These two neurochemically different areas of striatum respond differently to drug administration, so it is possible that some variance in MSN response may be explained by spatial locations that we were not able to measure.

*Further Directions*

Costa and colleagues (2006) showed that cells in a dopamine-depleted striatum aligned with large fluctuations in the LFP, an effect not present otherwise. We are currently investigating changes in spike-timing with respect to both local and spatially distributed striatal rhythms. Preliminary results suggest that FSIs can change the rhythms to which they entrain, and also the strength of that entrainment after pharmacological manipulation.

References

Albin et al. The functional anatomy of basal ganglia disorders. Trends in Neurosciences (1989) vol. 12 (10) pp. 366

Berke et al. Oscillatory entrainment of striatal neurons in freely moving rats. Neuron (2004) vol. 43 (6) pp. 883-896

Berke and Hyman. Addiction, dopamine, and the molecular mechanisms of memory. Neuron (2000) vol. 25 (3) pp. 515-532

Boyson et al. Quantitative autoradiographic localization of the D1 and D2 subtypes of dopamine receptors in rat brain. J Neurosci (1986) vol. 6 (11) pp. 3177-88

Costa et al. Rapid alterations in corticostriatal ensemble coordination during acute dopamine-dependent motor dysfunction. Neuron (2006) vol. 52 (2) pp. 359-369

Czubayko and Plenz. Fast synaptic transmission between striatal spiny projection neurons. Proc Natl Acad Sci USA (2002) vol. 99 (24) pp. 15764-9

Ferrari and Giuliani. Behavioural assessment in rats of the antipsychotic potential of the potent dopamine D2 receptor antagonist,(-) eticlopride. Pharmacological Research (1995) vol. 31 (5) pp. 261-267

Gerfen. The neostriatal mosaic: compartmentalization of corticostriatal input and striatonigral output systems. Nature (1984) vol. 311 (5985) pp. 461-464

Gerfen and Wilson. The basal ganglia. Handbook of chemical neuroanatomy (1996) vol. 12 (Part III) pp. 371-468

Haracz et al. Striatal single-unit responses to amphetamine and neuroleptics in freely moving rats. Neuroscience and Biobehavioral Reviews (1993) vol. 17 (1) pp. 1-12

Haracz et al. Amphetamine-induced excitations predominate in single neostriatal neurons showing motor-related activity. Brain Res (1989) vol. 489 (2) pp. 365-8

Kalanithi et al. Altered parvalbumin-positive neuron distribution in basal ganglia of individuals with Tourette syndrome. Proc Natl Acad Sci USA (2005) vol. 102 (37) pp. 13307-12

Kawaguchi. Physiological, morphological, and histochemical characterization of three classes of interneurons in rat neostriatum. J Neurosci (1993) vol. 13 (11) pp. 4908-23

Kawaguchi. Neostriatal cell subtypes and their functional roles. Neurosci Res (1997) vol. 27 (1) pp. 1-8

Kish et al. Multiple single-unit recordings in the striatum of freely moving animals: effects of apomorphine and D-amphetamine in normal and unilateral 6-hydroxydopamine-lesioned rats. Brain Res (1999) vol. 833 (1) pp. 58-70

Koós and Tepper. Inhibitory control of neostriatal projection neurons by GABAergic interneurons. Nat Neurosci (1999) vol. 2 (5) pp. 467-72

Leckman et al. Annotation: Tourette syndrome: a relentless drumbeat - driven by misguided brain oscillations. J Child Psychol & Psychiat (2006) vol. 47 (6) pp. 537-550

Mallet et al. Feedforward inhibition of projection neurons by fast-spiking GABA interneurons in the rat striatum in vivo. Journal of Neuroscience (2005) vol. 25 (15) pp. 3857-3869

Mukhopadhyay and Ray. A new interpretation of nonlinear energy operator and its efficacy in spike detection. IEEE transactions on bio-medical engineering (1998) vol. 45 (2) pp. 180-7

Nakano et al. Neural circuits and functional organization of the striatum. Journal of Neurology (2000) vol. 247 (17) pp. 1-15

Plenz. When inhibition goes incognito: feedback interaction between spiny projection neurons in striatal function. Trends in Neurosciences (2003) vol. 26 (8) pp. 436-43

Rebec et al. Responses of neurons in dorsal striatum during amphetamine-induced focused stereotypy. Psychopharmacology (Berl) (1997) vol. 130 (4) pp. 343-51

Tepper et al. GABAergic microcircuits in the neostriatum. Trends in Neurosciences (2004) vol. 27 (11) pp. 662-669

Tunstall et al. Inhibitory interactions between spiny projection neurons in the rat striatum. J Neurophysiol (2002) vol. 88 (3) pp. 1263-9

Voorn et al. Putting a spin on the dorsal-ventral divide of the striatum. Trends in Neurosciences (2004) vol. 27 (8) pp. 468-74

Wang and Rebec. Neuronal and behavioral correlates of intrastriatal infusions of amphetamine in freely moving rats. Brain Res (1993) vol. 627 (1) pp. 79-88

Weiner et al. Expression of muscarinic acetylcholine and dopamine receptor mRNAs in rat basal ganglia. Proc Natl Acad Sci USA (1990) vol. 87 (18) pp. 7050-4

West et al. Low-dose amphetamine elevates movement-related firing of rat striatal neurons. Brain Res (1997) vol. 745 (1-2) pp. 331-335

Wiltschko et al. Wavelet filtering before spike detection preserves waveform shape and enhances single-unit discrimination. Journal of Neuroscience Methods (2008) vol. 173 (1) pp. 34-40

## Acknowledgment

For involvement in completing the first chapter of this thesis, I thank Vaughn Hetrick and Michael Churchill for skilled technical assistance, and Loren Frank for suggesting and help implementing the Bessel filter. Support for this work came from the Tourette Syndrome Association, the Whitehall Foundation, and the National Institute on Drug Abuse.

For the second chapter, I thank Jeffrey Pettibone for performing surgeries and histology, and Vaughn Hetrick for maintaining recording equipment.

I thank Greg Gage for careful and thorough critiques of analyses, and for the late night company while neck-deep in data.

Many thanks to Joshua Berke for his time and effort teaching me how science is really done, both by example and honest critique.

Last, I would like to thank Marianna Anderle de Sylor for her loving support throughout the entire thesis process, for her fresh perspective on my work, and for helping me realize when it’s time to sleep and eat.

## Figure Captions

Figure 1. Identification of striatal cell subpopulations. A. Characteristics from wavelet-filtered waveforms were analyzed. In line with previous studies, FSIs were identified as units with peak widths at half-maximum between 50 and 200 μs, and peak-to-valley distances between 100 and 455 μs, with a baseline firing rate greater than 5Hz. MSNs were labeled as cells with peak widths between 150 and 450 μs, and peak-to-valley times between 560 and 1500 μs. Units that did not fit either criteria were not analyzed. B. Example MSN with a wide peak and long peak-to-valley time. C. Example FSI with short peak width and peak-to-valley time.

Figure 2. Firing rate changes for selected striatal neurons. A. Brain location and mean waveform ±1 S.D. of one FSI and two MSNs. The same FSI was recorded under both amphetamine and eticlopride manipulation. B. Binned firing rates before and after drug treatment. Spikes were binned into a time series using a 1 minute window, and then smoothed with a 3-point Gaussian kernel. Gaps in the trace occur when recording was paused to untangle recording cables. Saline and drug injections were given at 30 and 90 minutes, respectively. We analyzed firing rates in the saline and drug blocks starting 10 minutes after injection. C. Median firing rates after saline injection are in green, and drug injection are in red. Error bars indicate median absolute deviation and the scale is the same as the firing rate traces. Each change is significant for $p < 10\text{-}5$.

Figure 3. Population firing rate changes. A. Effect of amphetamine on FSI firing rate. Firing rates are calculated as the median spikes / s of a binned and smoothed time-series in a treatment block (see Methods). Filled circles indicate a significant change between treatments ($p < 0.01$, Mann-Whitney U Test), and open circles indicate no significant change. The bar plot summarizes the

number of FSIs that fall into the no significant change (NC), significant increase (Incr) or decrease (Decr) categories. B. The effect of eticlopride on FSI firing rates C. The effect of amphetamine on MSN firing rate. MSNs tend to increase firing rate after amphetamine, but much less robustly than FSIs. D. The effect of eticlopride on MSN firing rates. Again, MSNs exhibit a weaker but similar trend as FSIs under eticlopride.

Figure 4. Firing rate changes throughout the striatum. A. FSI firing rate changes induced by amphetamine and eticlopride. B. FSI firing rate changes for both eticlopride (black) and amphetamine (grey) show no clear relation to brain location. Significant changes (see Methods) are designated by circles, insignificant changes by triangles. C. MSN firing rate changes induced by amphetamine and eticlopride. D. MSNs also do not show a strong relationship between firing rate change and brain location.

Figures

Figure 1.

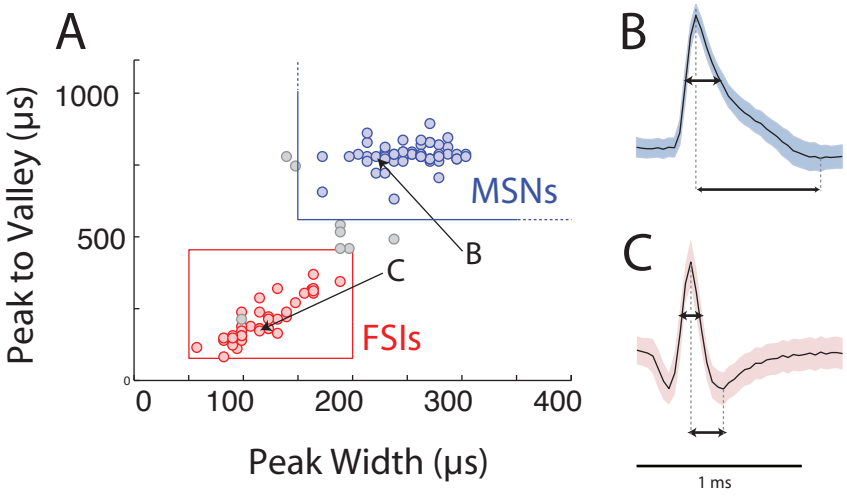


Figure 2.

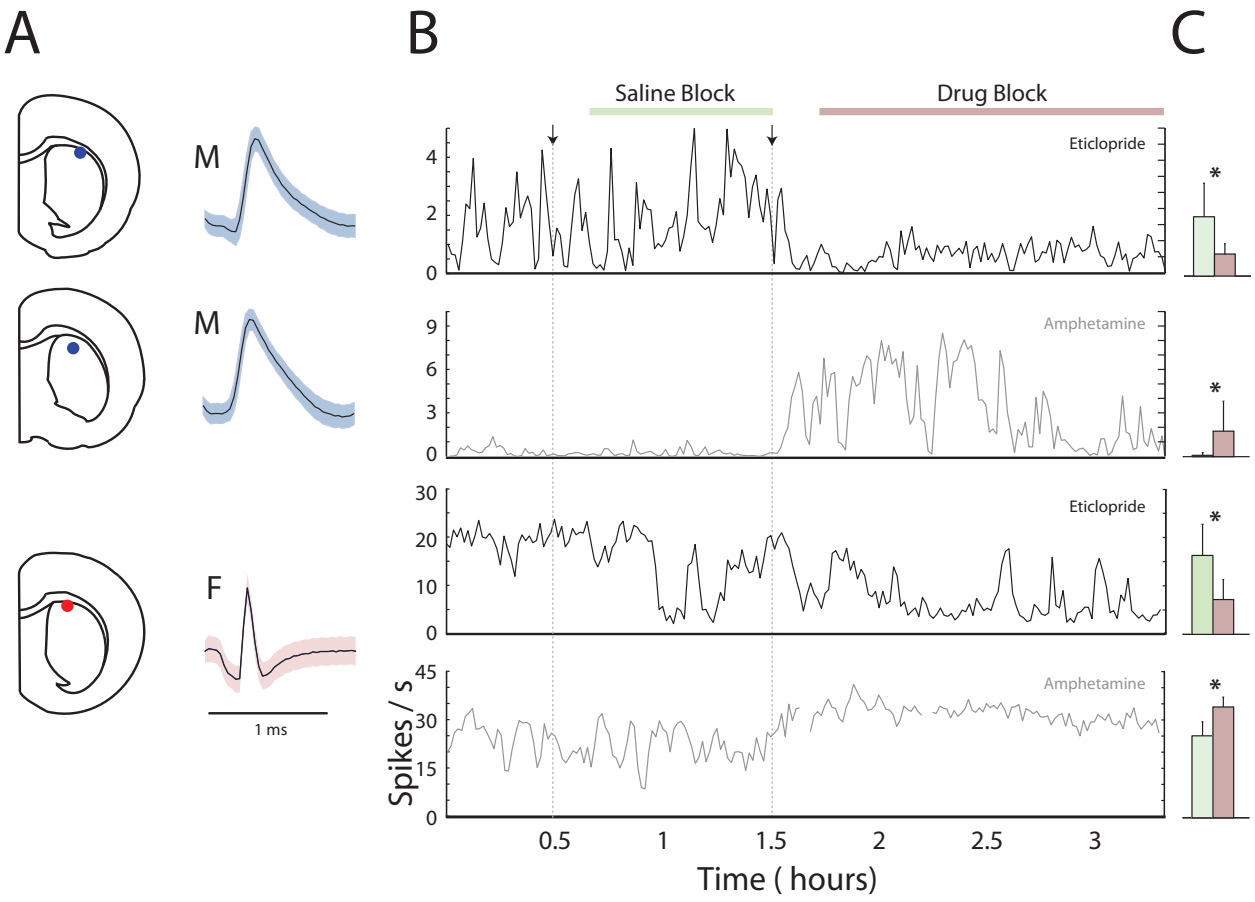
A
B
C
M
M
F
1 ms
Saline Block
Drug Block
Eticlopride
Amphetamine
Eticlopride
Amphetamine
Spikes / s
Time ( hours)
0.5
1
1.5
2
2.5
3

Figure 3.

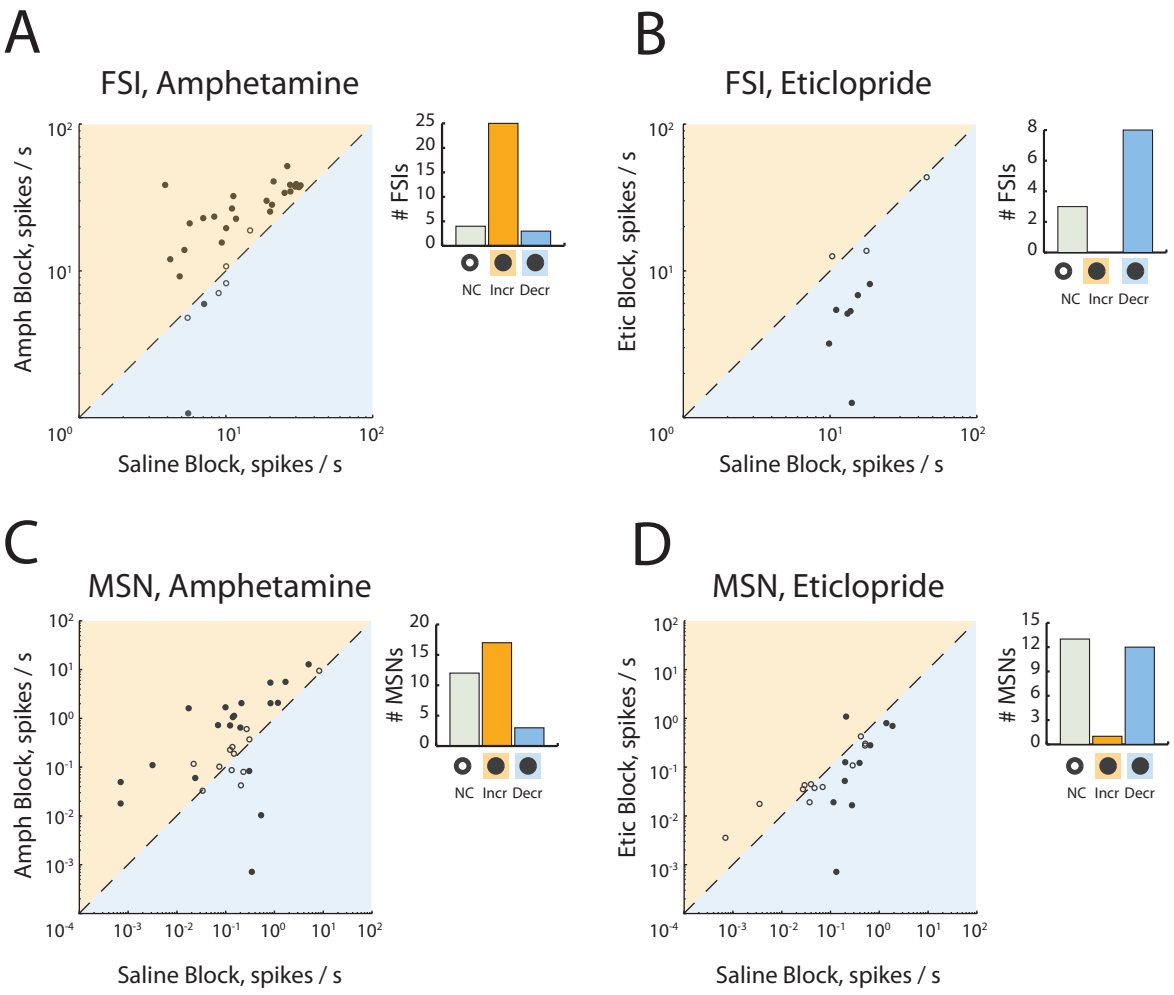
A
FSI, Amphetamine
Amph Block, spikes / s
Saline Block, spikes / s
# FSIs
NC Incr Decr
B
FSI, Eticlopride
Etic Block, spikes / s
Saline Block, spikes / s
# FSIs
NC Incr Decr
C
MSN, Amphetamine
Amph Block, spikes / s
Saline Block, spikes / s
# MSNs
NC Incr Decr
D
MSN, Eticlopride
Etic Block, spikes / s
Saline Block, spikes / s
# MSNs
NC Incr Decr

Figure 4.

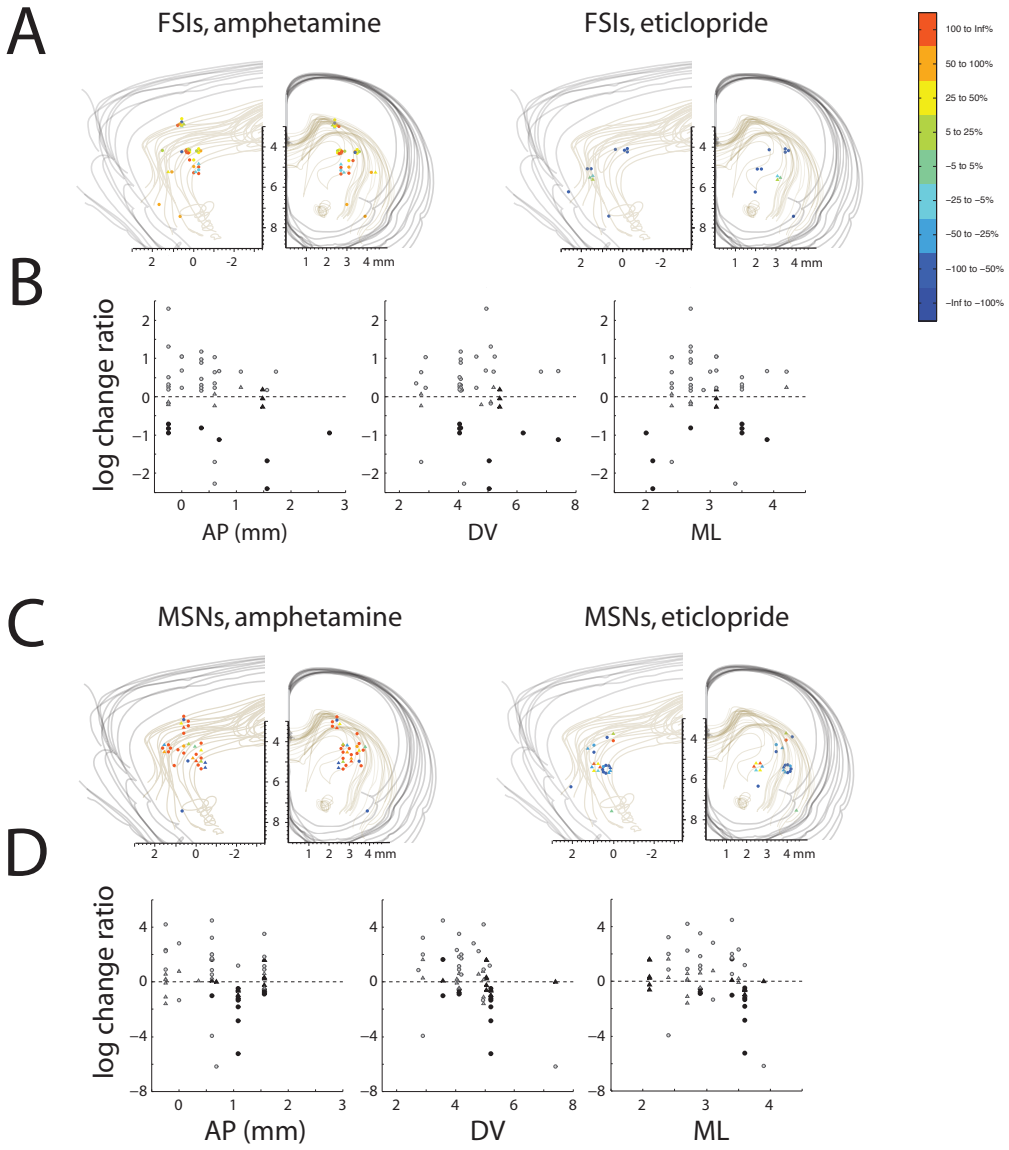
A
FSIs, amphetamine
FSIs, eticlopride
100 to Inf%
50 to 100%
25 to 50%
5 to 25%
−5 to 5%
−25 to −5%
−50 to −25%
−100 to −50%
−Inf to −100%
4 mm
B
log change ratio
AP (mm)
DV
ML
C
MSNs, amphetamine
MSNs, eticlopride
D
log change ratio
AP (mm)
DV
ML